ARTICLE OPEN

Check for updates

Transport behaviors of topological band conduction in $KTaO_3$'s two-dimensional electron gases

Yuting Zou[1,2,6], Hyungki Shin[3,4,6], Haoran Wei[1,2], Yiyan Fan[1,2], Bruce A. Davidson[3,4], Er-Jia Guo[1,2,5], Qihong Chen[1,2,5], Ke Zou[3,4]✉ and Zhi Gang Cheng[1,2,5]✉

Two-dimensional electron gas systems (2DEGs) generated at the oxide interfaces that exhibit rich physics phenomena opened up an era for oxide-based electronics, photonics, and spintronics. The recent discovery of superconductivity plus the strong spin-orbital coupling naturally existing in the 2DEGs of $KTaO_3$ (KTO) made KTO an exciting platform for the interplay of the electronic and spin degrees of freedom to create exotic physical properties. By directly placing KTO's 2DEGs next to another strongly-correlated oxide with nontrivial topological nodes, we reveal the anomalous effects which were induced by the topological states in the electronic transport properties of the KTO's 2DGEs, due to the electronic reconstruction caused by the proximity effect. This adds an additional prospect to the functions of KTO heterostructures.

npj Quantum Materials (2022)7:122 ; https://doi.org/10.1038/s41535-022-00536-5

INTRODUCTION

Intensive attentions have recently been focused on perovskite oxide heterostructures for two-dimensional electron gases (2DEGs) hosted at interfaces. A rich variety of exotic phenomena has been observed, such as metal-insulator transitions (MITs), magnetic correlations, strong tunability by an electric field, and superconductivity. A typical example is $LaAlO_3/SrTiO_3$ (LAO/STO) within which 2DEGs is formed in STO close to the interface by charge transfer due to discontinuity of polarity. It simultaneously exhibits extremely high mobility (10,000 $cm^2 V^{-1} s^{-1}$), superconductivity, ferromagnetism, and a rich electronic phase diagram[1–7]. Especially, the coexistence of ferromagnetism and superconductivity makes LAO/STO an intriguing candidate for unconventional superconductivity. In addition, Rashba-type spin-orbit coupling (SOC) associated with broken spatial inversion symmetry provides a convenient and promising way to manipulate magnetic structure electrically, making LAO/STO an ideal platform for practice in spintronics[8].

With respect to STO, $KTaO_3$ (KTO) shares similarities but also distinct features in the crystal structure, transport properties, and band structure[9–11]. KTO-based heterostructures accordingly host 2DEGs when oxygen vacancies are generated in KTO. Some in this series exhibit high mobility, strong spin polarization, and the recently discovered non-conventional superconductivity, etc[12–19]. In particular, compared with STO-based counterparts for which Ti *3d* orbitals make the main contributions, KTO-based heterostructures incorporate itinerant electrons from Ta *5d*-orbitals. Stronger SOC is thus expected to introduce non-zero Berry curvature to the reciprocal space[20]. Topological band structures and other phenomena such as Rashba splitting may occur consequently. A recent study successfully demonstrates the simultaneous tunability of superconductivity and SOC of an EuO/KTO heterostructure using electric field effect[19]. It was also pointed out further by a recent theoretical study that topological superconductivity may be induced by in-plane magnetic field to a two-dimensional metallic system with SOCs because SOC creates topologically nontrivial spin textures and could also serve as attractive force for electron parings[21].

Non-trivial topology, together with existing exotic properties including superconductivity and spin polarization, enriches KTO-based heterostructure with great perspective in both fundamental research and practical applications. For instance, topological superconductivity is theoretically proved to be able to host Majorana zero modes—an essential prerequisite to realizing non-Abelian statistics—and potentially play a key role in developing topological quantum computations[22]. Moreover, the strong SOC can also be used in developing spintronic devices such as spin-orbit torque-based magneto-resistive randomized access memory (SOT-MRAM), making KTO-based heterostructure a better candidate for spintronics compared with its STO-based counterpart.

High mobility is the most precious property for 2DEGs for both studies on fundamental physical science and development of practical devices. It is reported that highly mobile and spin-polarized 2DEG could be realized within the heterostructure of EuO/KTO[23] based on which thermal spin injection was realized[13] and superconductivity was observed[15,17,24], for which the 2DEG is restricted near the EuO/TaO_2 interface. Alternatively, such an interface could also exist within the heterostructure $EuTiO_3/KTaO_3$ (ETO/KTO), whereas $EuTiO_3$ (ETO) has distinctive magnetic properties due to the partially-filled *4 f* orbitals of Eu and their exchange interaction between Ti-*3d* and Eu-*5d* orbitals[25]. G-type antiferromagnetism is formed at a Néel temperature of $T_N = 5.5$ K with *7 μB* on each Eu^{2+} site[26,27] (see Fig. 1a). Moreover, multiferroics due to strong spin-lattice coupling has been shown by first-principle calculations[28] and strain-effect[29]. Recent experiments reveal evidence of the existence of topology-related phenomena including skyrmion-like Hall effect[30] and Weyl nodes[26] in doped ETO.

Here we report on our studies on the electric transport measurements on ETO/KTO heterostructures. The studies were conducted in comparison with $LaTiO_3/KTaO_3$ (LTO/KTO) which was

[1]Beijing National Laboratory for Condensed Matter Physics and Institute of Physics, Chinese Academy of Sciences, 100190 Beijing, China. [2]School of Physical Sciences, University of Chinese Academy of Sciences, 100190 Beijing, China. [3]Department of Physics and Astronomy, University of British Columbia, Vancouver, BC V6T 1Z1, Canada. [4]Quantum Matter Institute, University of British Columbia, Vancouver, BC V6T 1Z4, Canada. [5]Songshan Lake Materials Laboratory, Dongguan 523808 Guangdong, China. [6]These authors contributed equally: Yuting Zou, Hyungki Shin. ✉email: kzou@phas.ubc.ca; zgcheng@iphy.ac.cn

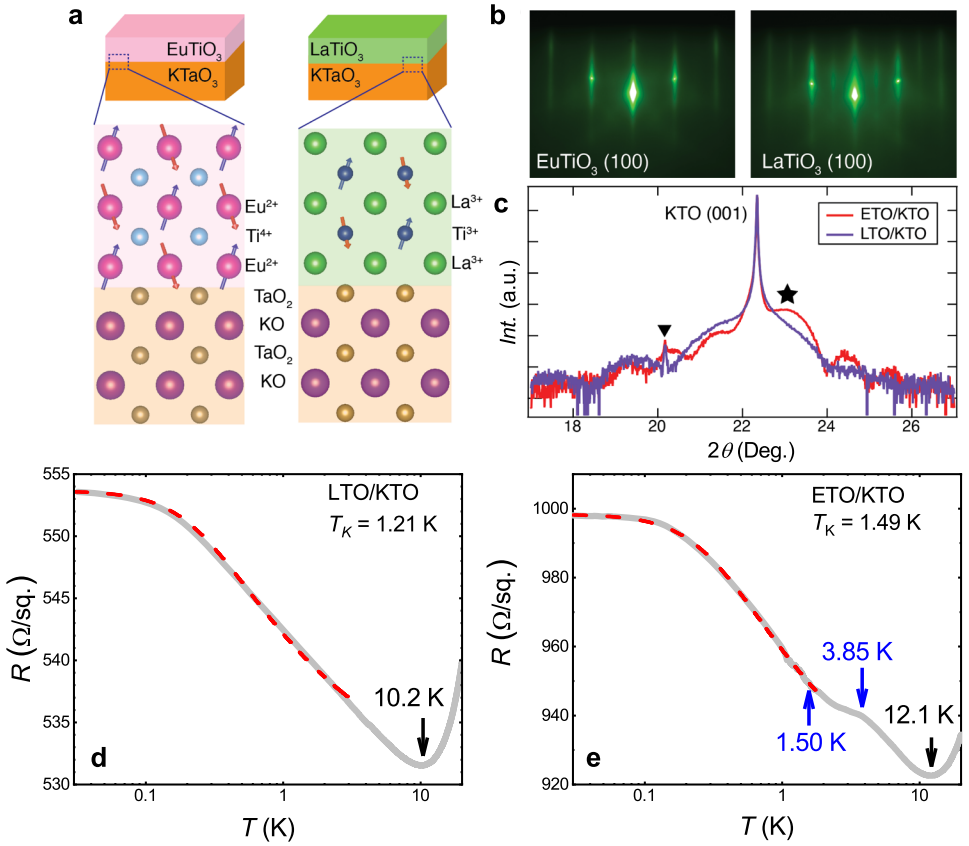

Fig. 1 Structural characterizations and temperature dependence of resistivity for heterostructures of ETO/KTO and LTO/KTO. a Schematic picture of ETO/KTO (left) and LTO/KTO (right) heterostructures and their atomic and antiferromagnetic spin structures (below). The size of spins on the Eu^{2+} and Ti^{3+} indicates the relative magnitude of magnetic moments ($7\mu_B$/Eu and $0.5\mu_B$/Ti). **b** In-situ reflection high-energy electron diffraction (RHEED) intensity picture of ETO and LTO after 10 u.c. growth. **c** XRD scan of 20 u.c. ETO/KTO (red) and 10 u.c. LTO/KTO (purple). The symbol ★ and ▼ indicate the (001) peak of ETO and carbon paste defect, respectively. Temperature dependence of resistivity is plotted in (**d**) for LTO/KTO and in (**e**) for ETO/KTO.

reported to also host 2DEG with high mobilities[14]. LTO and ETO were deposited onto substrates of KTO respectively by the molecular beam epitaxy (MBE) method. We observed Kondo effects for the temperature dependence of resistivity and corrections to magnetoresistance due to superposition of weak anti-localization (WAL) and weak localization (WL) for both samples. The extracted SOC length l_{SO} is significantly smaller for ETO/KTO in comparison with LTO/KTO, suggesting different origins of SOC for these two heterostructures. Since Rashba effect should be similar for both heterostructures as both 2DEGs reside in KTO, the difference should originate from the proximity effect of the topological band structure of ETO, which is furtherly supported by its anomalous Hall effect. Our results provide an effective way for tuning and engineering topological properties of band structure into KTO-based heterostructure which can be extended to other interfacial electronic systems.

RESULTS

Temperature-dependence of resistivity

Samples were prepared by MBE method and high crystalline quality was achieved (see Fig. 1b and c). Both samples have shown the typical densities of 2DEG carriers in KTO (Supplementary Fig. 2) contributed by the oxygen vacancies formed during the high temperature annealing and the electronic reconstruction due to the polar nature of KTO[20]. Although polar catastrophe has been proposed to be another origin of 2DGEs, experimental evidence remains missing. To confirm the reported results are caused by intrinsic properties and to check their sample-dependence, we also prepared a batch of samples using pulsed-laser deposition (PLD) method. The experimental results of these samples are discussed in Supplementary Note 3.

Figure 1d and e exhibits the temperature dependence of resistivity below 20 K. Both samples exhibit metal-insulator transitions. For LTO/KTO, the transition takes place at 10.2 K, below which it firstly exhibits an upturn with an approximate ln(T) dependence, and starts to saturate from 300 mK down to 30 mK. Such a temperature dependence is characteristic of Kondo effect originating from the interplay of itinerant electrons and magnetic impurities, and the saturation is caused by screening of magnetic impurities by bound electrons via spin-exchange interactions. The temperature dependence can be fitted by the empirical relation[31,32]

$$R(T) = R_0 + R_K(T) = R_0 + R_K(0)\left[\left(\frac{T}{T_K}\right)^2\left(2^{\frac{1}{s}}-1\right)+1\right]^{-s} \quad (1)$$

where R_0 is temperature independent resistance including residual resistance due to sample disorder and extra resistance associated with WL or WAL, T_K the Kondo temperature, and s a parameter related with spin. Here we fix $s = 0.22$ for spin $S = 1/2$[32] and achieve a satisfactory fitting with $T_K = 1.21$ K. In comparison, the ETO/KTO exhibits the metal-insulator transition at 12.1 K and a well-fitted Kondo behavior below 1.50 K with $s = 0.22$ and $T_K = 1.49$ K. There are two wiggle points at 3.85 K and 1.50 K, which lead to the resistance below 1.50 K shifting downwards. The shift may be ascribed to the suppression of electron back-scattering associated

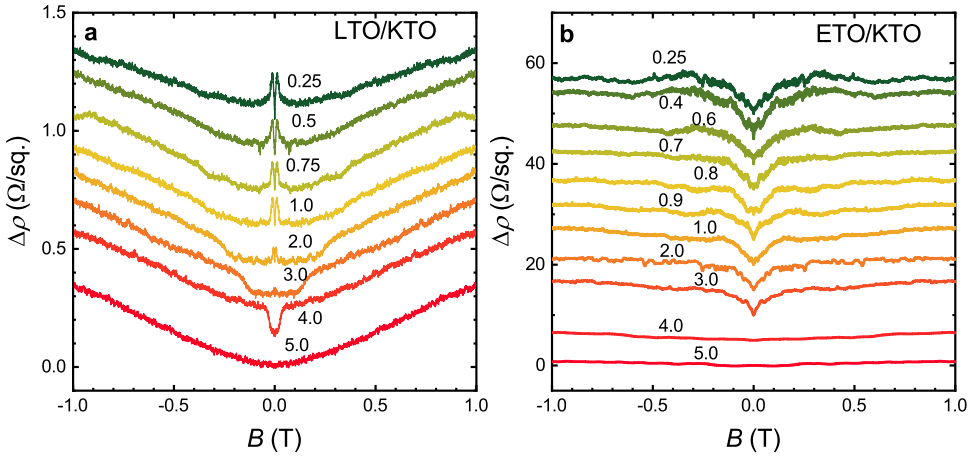

Fig. 2 Magnetoresistivity (MR) of LTO/KTO and ETO/KTO. MR is given by $\Delta\rho = \rho(B) - \rho(0)$ for LTO/KTO plotted in (**a**) and ETO/KTO plotted in (**b**). Curves are vertically shifted for clarity, and temperatures for each MR curve are labeled.

with the emergence of topology to conducting band, which will be discussed later.

Localization effects to magnetoresistance

To explore the effects of spin-orbital couplings, magnetoresistance (MR) has been measured for both samples at multiple temperatures (see Fig. 2). LTO/KTO demonstrates a sharp feature within the narrow range of ±0.05 T at 0.25 K. With an increasing magnetic field, resistivity firstly increases and starts to decrease for $|B| > 0.015$ T. Such a feature becomes less obvious as the temperature is raised and vanishes at around 3 K. In addition, an extra dip of resistance is observed at 4 K with a half-width of 0.05 T. The dip develops into a plateau with larger width and smoother edge at lower temperatures, and eventually merges with the universal background. This phenomenon is indeed puzzling. One possibility is that the LTO/KTO becomes superconducting at 4 K, but so far superconductivity has been realized only in (110)- and (111)-oriented EuO/KTO[15] and LAO/KTO[16] heterostructures. Therefore, more investigations are required to understand this phenomenon. As for ETO/KTO, a similar feature is observed in a similar temperature range but with much larger magnitude and much wider magnetic field range, extending to ±0.5 T. However, no additional plateau feature is observed.

The superposition of positive and negative MR suggests the coexistence of WL and WAL[33]. In the diffusive transport process at zero magnetic field, WL originates from the phase coherence of in-coming and out-going electrons, therefore leading to an enhancement of back-scattering probability and an increase in resistivity. In contrast, WAL is associated with the existence of SOC that brings an extra phase of π, which converts the interference to be destructive and leads to a decrease in resistivity. These extra corrections are suppressed as magnetic field increases since phase coherence is destroyed. Corrections of WL and WAL to magnetoconductivity can be described by the theory of Iordanskii, Lyanda-Geller, and Pikus (ILP)[34]

$$\Delta\sigma(B) = -\frac{e^2}{\pi h}\left[\frac{1}{2}\psi\left(\frac{1}{2}+\frac{B_\phi}{B}\right) - \frac{1}{2}\ln\left(\frac{B_\phi}{B}\right) - \psi\left(\frac{1}{2}+\frac{B_\phi+B_{SO}}{B}\right) + \ln\left(\frac{B_\phi+B_{SO}}{B}\right) - \frac{1}{2}\psi\left(\frac{1}{2}+\frac{B_\phi+2B_{SO}}{B}\right) + \frac{1}{2}\ln\left(\frac{B_\phi+2B_{SO}}{B}\right)\right] \quad (2)$$

where $B_\phi = \frac{\hbar}{4el_\phi^2}$ is the dephasing magnetic field characterized by the phase coherence length l_ϕ, $B_{SO} = \frac{\hbar}{4el_{SO}^2}$ is the spin-orbit scattering field characterized by the spin-orbit scattering length l_{SO}, and $\psi(x)$ is digamma function. We find that Eq. (2) can fit the MR very well for both samples as shown in Fig. 3a–d and Fig. 4a–d, respectively. The extracted values of l_ϕ and l_{SO} are plotted in Fig. 3e and Fig. 4e for each sample. On one hand, these two characteristic lengths share some properties in common: l_ϕ scales with $T^{-1/2}$ where the exponent of −1/2 indicates a two-dimensional transport process, and l_{SO} is not obviously temperature-dependent; On the other hand, l_ϕ and l_{SO} for LTO/KTO ($l_\phi = 200 \sim 232$ nm and $l_{SO} \approx 190$ nm) are significantly larger than those for ETO/KTO ($l_\phi = 130 \sim 180$ nm and $l_{SO} \approx 50$ nm), in consistency with previous measurements of 5d perovskite oxides[35]. In comparison, mean free path (l_{mfp}) of electron drifts are significantly smaller, ~20 nm for both samples (see Supplementary Fig. 2). Given that the ILP theory is derived for the diffusive regime, i.e., $B < \frac{\hbar}{2el_{mfp}^2}$, the value of l_{mfp} constrains the validity of the ILP model within the magnetic field of ±0.8 T, in consistence with the fitting for ETO/KTO. However, it is limited in a much smaller range for LTO/KTO, probably because spin canting caused by external field are more obvious due to the smaller magnetic moment of Ti^{3+}[14,27].

The fact that l_ϕ being larger than l_{SO} guarantee the phase coherence during the spin-orbit scattering processes, which leads to the obvious positive MR (or negative magnetoconductance) associated with the WAL effect. We note that the magnitude of conductance correction $\Delta\sigma$ for LTO/KTO ($\sim 0.01e^2/h$) is about one order of magnitude smaller than that for ETO/KTO ($\sim 0.2e^2/h$) (see Supplementary Figs. 3 and 4). This is because the difference between l_ϕ and l_{SO} is much smaller ($\frac{l_\phi}{l_{SO}} \approx 1.1$ for LTO/KTO vs. 3.0 for ETO/KTO), and the effects of WL partially cancel that of WAL on conductance. Furthermore, both l_ϕ and l_{SO} for LTO/KTO are significantly larger than ETO/KTO, suggesting either much more scattering sites existing in the ETO/KTO sample to destroy phase coherence and to cause spin flips, or the transport process is governed by different nature of conducting band. The former is unlikely thanks to the similar quality of crystalline and interfaces for both samples while the latter is possible. Considering that Rashba coupling should be similar for both cases, the difference could originate from the much larger magnetic moment on Eu^{2+} sites and the possible topological band of ETO[26].

Anomalous hall effect

To clarify the origin of the stronger scattering in the ETO/KTO sample, we performed Hall measurements for both samples (Supplementary Fig. 1 and 5). In spite of the quasi-linear dependence of ρ_{xy} on the magnetic field, a weak anomalous Hall effect can still be observed. Figure 5 shows the anomalous Hall resistance (AHE) ρ_{AHE} extracted by subtracting ρ_{xy} with an ordinary linear Hall term $\rho_H \propto aB$ for which a is a coefficient determined by a linear fit of ρ_{xy} between 3 T and 4 T. In stark

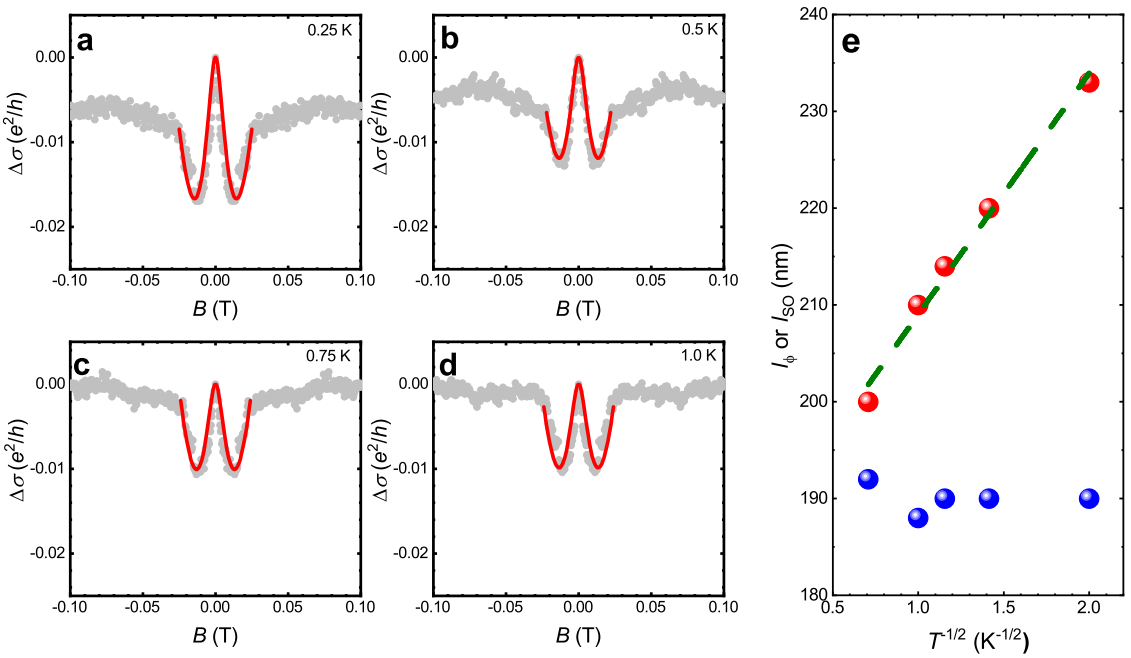

Fig. 3 Fitting of the magnetoconductance (MC) of LTO/KTO. a–d MC at various temperatures. Gray dots are experimental data and red solid lines are fitting curves based on ILP theory. **e** The extracted l_ϕ (red symbols) and l_{SO} (blue symbols) plotted against $T^{-\frac{1}{2}}$. The green dashed line is a linear fit.

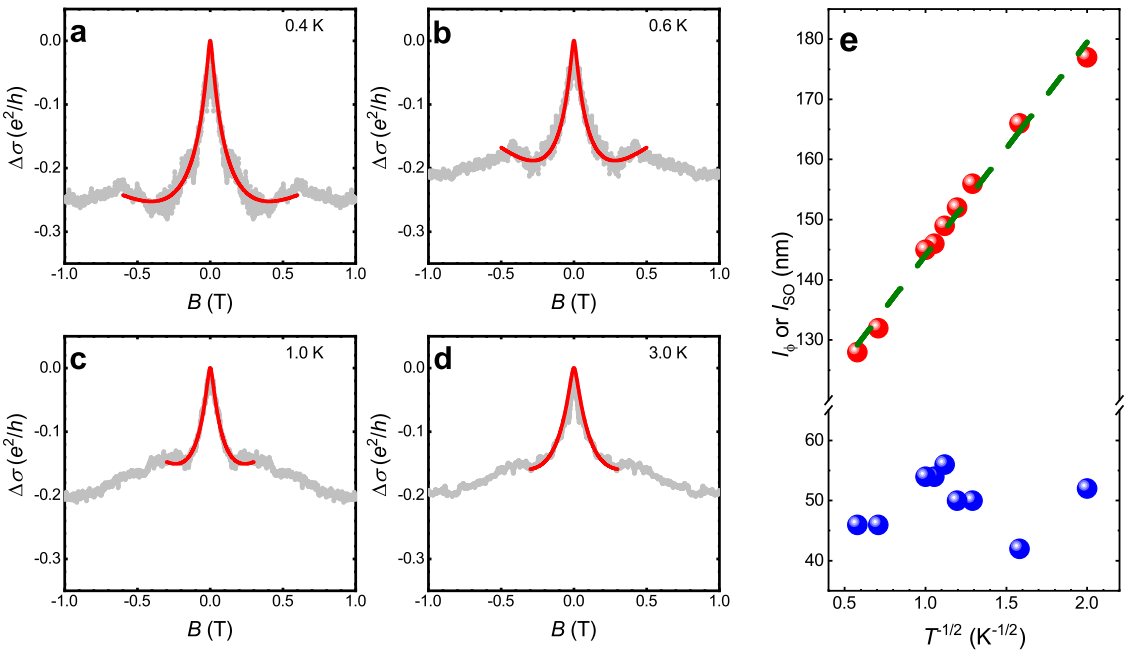

Fig. 4 Fitting of the MC of ETO/KTO. a–d MC at various temperatures. Gray dots are experimental data and red solid lines are fitting curves based on ILP theory. **e** The extracted l_ϕ (red symbols) and l_{SO} (blue symbols) plotted against $T^{-\frac{1}{2}}$. The green dashed line is a linear fit.

contrast, ρ_{AHE} for LTO/KTO is negative (namely $\rho_{AHE} < 0$ for $B > 0$) and temperature-independent below 5 K, while ρ_{AHE} for ETO/KTO is positive and exhibits a strong temperature dependence below 5 K. Its magnitude—at 0.5 K for example—is about 10 times larger than that of LTO/KTO.

DISCUSSION

In Fig. 5b, we find that ρ_{AHE} at 2 K saturates at about 2 T. This is consistent with the magnetization measurements of ETO[26,36]. The onset temperature of ρ_{AHE} is also close to the Néel temperature of ETO ($T_N = 5.5$ K). Both evidences support that the AHE is highly related with the proximity of ETO. It has been pointed out that non-trivial Berry curvature can be induced and controlled in ETO by applying external magnetic field[26]. Induced Zeeman splitting in the process of canting magnetic moments causes type II Weyl nodes and topologically changes the band structure of ETO. The high similarity between the measured ρ_{AHE} and magnetization in ETO suggests that the 2DEG at the ETO/KTO interface is influenced by the topological band structure of ETO.

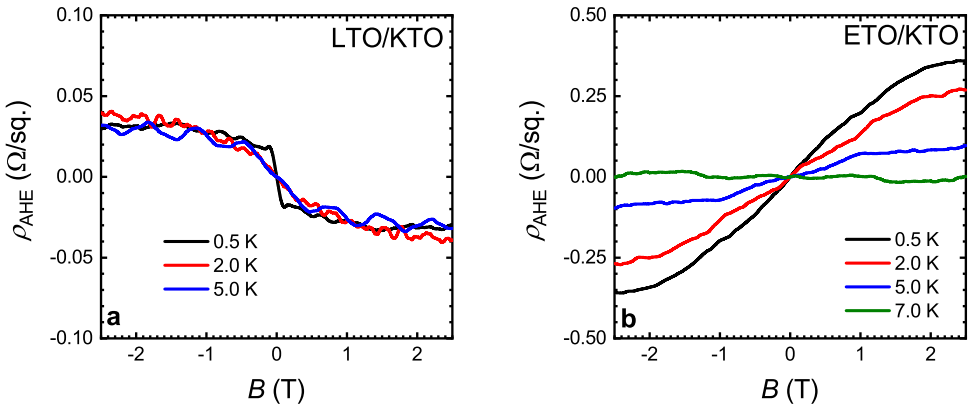

Fig. 5 Anomalous Hall effect. Anomalous Hall resistivity for LTO/KTO is plotted in (**a**) and that for ETO/KTO is plotted in (**b**).

The emergence of ρ_{AHE} also coincides with the wiggle points appearing in the ρ–T curve in Fig. 1e. The appearance of wiggle points could be due to the suppression of electron back-scattering associated with spin-orbit locking. In contrast, ρ_{AHE} for LTO/KTO, being temperature independent and smaller in magnitude, should solely stem from the Rashba-type SOC in KTO since the Rashba effect is weakly temperature dependent below 5 K because of its higher spin-orbit split band[35,37].

In summary, we have studied the transport properties of 2DEGs residing near the interfaces of both LTO/KTO and ETO/KTO heterostructures, and observed superposition of WL and WAL effects. The extracted phase coherence length l_ϕ scales with $T^{-\frac{1}{2}}$ while l_{SO} is temperature independent, confirming the existence of SOC in both heterostructures. Smaller values of l_ϕ and l_{SO} for ETO/KTO imply that the microscopic origins of SOC are different and the transport process is governed by different nature of conducting band. By analyzing the anomalous Hall effect, we found that AHE for ETO/KTO features with a positive sign, strong temperature dependence, and larger magnitude, all different from those of LTO/KTO. We state that such differences, together with the localization effects, stem from the strong topological band induced by the proximation of the ETO film.

METHODS

Sample preparations and structural characterizations

All ETO and LTO films were grown on insulating KTO (001) substrates (MTI). The lattice constant of KTO is 3.99 Å, larger than ETO (3.905 Å) and LTO (3.97 Å), which results in the tensile strain in all epitaxial films.

The samples were grown in an oxide molecular beam epitaxial (MBE) system (Veeco GenXplor) with a base pressure $<5\times10^{-10}$ Torr. The flux ratio between Eu, La, and Ti was calibrated by quartz crystal microbalance, and the film growth process and the number of layers were monitored and determined by in-situ reflection high-energy electron diffraction.

At the temperature of 700 °C, KTO substrate was annealed for 30 min without oxygen to degas. After that, the ETO film was grown on the substrate by co-deposition in a partial pressure of molecular oxygen pressure of $4\sim5\times10^{-8}$ Torr. The LTO film was also grown by co-deposition in a partial pressure of molecular oxygen pressure of $3\sim4\times10^{-8}$ Torr. After growth, all samples were capped with 5 nm of amorphous Ge at room temperature to prevent sample deterioration during the ex-situ measurements. Bare KTO substrate, after the same annealing process and 5 nm of amorphous Ge capping, shows clear insulating behavior. Same growth methods generate insulating/stoichiometric ETO and LTO films on other insulating substrates.

After the growth and capping, the films were characterized by X-ray diffraction (XRD, Bruker) in the 2θ-ω mode for the structural information using Cu Kα1 radiation.

Additional samples were grown by pulsed-laser deposition (PLD) technique. The epitaxial thin films were fabricated on (100)-oriented KTO substrates. During thin-film fabrication, the laser fluence was 1.2–1.5 J cm^{-2}, the repetition rate was 5 Hz, and the temperature of the substrate was kept at 750 °C. The films were grown under high vacuum conditions with a typical growth pressure of $\sim1\times10^{-6}$ Torr. After 3000 laser pulses, the films were cooled down to room temperature in a vacuum at a rate of -15 °C min^{-1}.

Electrical transport measurements and data analyses

Electric transport measurements were performed on a home-made dilution refrigerator. Van der Pauw method was used for the transport measurements, with both LTO/KTO and ETO/KTO samples in a square shape with dimensions of 5×5 mm^2 and electric contacts made to four corners by indium-soldering. The standard lock-in technique was used with a frequency of 17 Hz and a current of 1 μA. Longitudinal resistance R_{xx} was measured by running current through two contacts on the same edge, and Hall resistance R_{xy} by running current through two contacts on diagonal. Due to the finite contact size and non-ideal symmetry, anti-symmetrization was performed to extract R_{xy}. Pictures were taken for the samples after the contacts were made based on which transport processes were then simulated by finite element modeling using COMSOL. The simulations were run with ρ_{xx} and ρ_{xy} as input parameters to match the experimental results.

DATA AVAILABILITY

All the presented data can be visited via the following link: https://doi.org/10.6084/m9.figshare.21731117.v1.

Received: 9 May 2022; Accepted: 23 December 2022;
Published online: 29 December 2022

REFERENCES

1. Ohtomo, A. & Hwang, H. Y. A high-mobility electron gas at the $LaAlO_3/SrTiO_3$ heterointerface. *Nature* **427**, 423–426 (2004).
2. Reyren, N. et al. Superconducting interfaces between insulating oxides. *Science* **317**, 1196–1199 (2007).
3. Brinkman, A. et al. Magnetic effects at the interface between non-magnetic oxides. *Nat. Mater.* **6**, 493–496 (2007).
4. Li, L., Richter, C., Mannhart, J. & Ashoori, R. C. Coexistence of magnetic order and two-dimensional superconductivity at $LaAlO_3/SrTiO_3$ interfaces. *Nat. Phys.* **7**, 762–766 (2011).

5. Caviglia, A. D. et al. Tunable Rashba spin-orbit interaction at oxide interfaces. *Phys. Rev. Lett.* **104**, 126803 (2010).
6. Caviglia, A. D. et al. Electric field control of the $LaAlO_3/SrTiO_3$ interface ground state. *Nature* **456**, 624–627 (2008).
7. Caviglia, A. D. et al. Two-dimensional quantum oscillations of the conductance at $LaAlO_3/SrTiO_3$ interfaces. *Phys. Rev. Lett.* **105**, 236802 (2010).
8. Herranz, G. et al. Engineering two-dimensional superconductivity and Rashba spin–orbit coupling in $LaAlO_3/SrTiO_3$ quantum wells by selective orbital occupancy. *Nat. Commun.* **6**, 6028 (2015).
9. Thompson, J. R., Boatner, L. A. & Thomson, J. O. Very low-temperature search for superconductivity in semiconducting $KTaO_3$. *J. Low. Temp. Phys.* **47**, 467–475 (1982).
10. Wemple, S. H. Some transport properties of oxygen-deficient single-crystal potassium tantalate ($KTaO_3$). *Phys. Rev.* **137**, A1575–A1582 (1965).
11. Mattheiss, L. F. Energy bands for $KNiF_3$, $SrTiO_3$, $KMoO_3$, and $KTaO_3$. *Phys. Rev. B* **6**, 4718–4740 (1972).
12. Zhang, H. et al. Highly mobile two-dimensional electron gases with a strong gating effect at the amorphous $LaAlO_3/KTaO_3$ interface. *ACS Appl. Mater. Interfac.* **9**, 36456–36461 (2017).
13. Zhang, H. et al. Thermal spin injection and inverse Edelstein effect of the two-dimensional electron gas at EuO-$KTaO_3$ interfaces. *Nano Lett.* **19**, 1605–1612 (2019).
14. Zou, K. et al. $LaTiO_3/KTaO_3$ interfaces: A new two-dimensional electron gas system. *APL Mater.* **3**, 036104 (2015).
15. Liu, C. et al. Two-dimensional superconductivity and anisotropic transport at $KTaO_3$ (111) interfaces. *Science* **371**, 716–721 (2021).
16. Chen, Z. et al. Electric field control of superconductivity at the $LaAlO_3/KTaO_3$(111) interface. *Science* **372**, 721–724 (2021).
17. Ma, Y. et al. Superconductor-metal quantum transition at the EuO/$KTaO_3$ interface. *Chin. Phys. Lett.* **37**, 117401 (2020).
18. Chen, Z. et al. Two-dimensional superconductivity at the $LaAlO_3/KTaO_3$(110) heterointerface. *Phys. Rev. Lett.* **126**, 026802 (2021).
19. Hua, X. et al. Tunable two-dimensional superconductivity and spin-orbit coupling at the EuO/$KTaO_3$(110) interface. *npj Quant. Mater.* **7**, 97 (2022).
20. Gupta, A. et al. $KTaO_3$ —The new kid on the spintronics block. *Adv. Mater.* **34**, 2106481 (2022).
21. Yuan, N. F. Q. & Fu, L. Topological metals and finite-momentum superconductors. *Proc. Natl Acad. Sci. USA* **118**, e2019063118 (2021).
22. Chung, S. B., Chan, C. & Yao, H. Dislocation Majorana zero modes in perovskite oxide 2DEG. *Sci. Rep.* **6**, 25184 (2016).
23. Zhang, H. et al. High-mobility spin-polarized two-dimensional electron gases at EuO/$KTaO_3$ interfaces. *Phys. Rev. Lett.* **121**, 116803 (2018).
24. Liu, C. et al. Tunable superconductivity at the oxide-insulator/$KTaO_3$ interface and its origin. Preprint at https://arxiv.org/abs/2203.05867 (2022).
25. Maruhashi, K. et al. Anisotropic quantum transport through a single spin channel in the magnetic semiconductor $EuTiO_3$. *Adv. Mater.* **32**, 1908315 (2020).
26. Takahashi, K. S. et al. Anomalous Hall effect derived from multiple Weyl nodes in high-mobility $EuTiO_3$ films. *Sci. Adv.* **4**, eaar7880 (2018).
27. Shin, H. et al. Controlling the electrical and magnetic ground states by doping in the complete phase diagram of titanate $Eu_{1-x}La_xTiO_3$ thin films. *Phys. Rev. B* **101**, 214105 (2020).
28. Fennie, C. J. & Rabe, K. M. Magnetic and electric phase control in epitaxial $EuTiO_3$ from first principles. *Phys. Rev. Lett.* **97**, 267602 (2006).
29. Lee, J. H. et al. A strong ferroelectric ferromagnet created by means of spin–lattice coupling. *Nature* **466**, 954–958 (2010).
30. Ahadi, K., Galletti, L. & Stemmer, S. Evidence of a topological Hall effect in $Eu_{1-x}Sm_xTiO_3$. *Appl. Phys. Lett.* **111**, 172403 (2017).
31. Lee, M., Williams, J. R., Zhang, S., Frisbie, C. D. & Goldhaber-Gordon, D. Electrolyte gate-controlled Kondo effect in $SrTiO_3$. *Phys. Rev. Lett.* **107**, 256601 (2011).
32. Costi, T. A. et al. Kondo decoherence: finding the right spin model for iron impurities in gold and silver. *Phys. Rev. Lett.* **102**, 056802 (2009).
33. Albright, S. D., Zou, K., Walker, F. J. & Ahn, C. H. Weak antilocalization in topological crystalline insulator SnTe films deposited using amorphous seeding on $SrTiO_3$. *APL Mater.* **9**, 111106 (2021).
34. Iordanskii, S. V., Lyanda-Geller, Yu. B. & Pikus, G. E. Weak localization in quantum wells with spin-orbit interaction. *JETP Lett.* **60**, 206–211 (1994).
35. Nakamura, H. & Kimura, T. Electric field tuning of spin-orbit coupling in $KTaO_3$ field-effect transistors. *Phys. Rev. B* **80**, 121308 (2009).
36. Takahashi, K. S., Onoda, M., Kawasaki, M., Nagaosa, N. & Tokura, Y. Control of the anomalous Hall effect by doping in $Eu_{1-x}La_xTiO_3$ thin films. *Phys. Rev. Lett.* **103**, 057204 (2009).
37. King, P. D. C. et al. Subband structure of a two-dimensional electron gas formed at the polar surface of the strong spin-orbit perovskite $KTaO_3$. *Phys. Rev. Lett.* **108**, 117602 (2012).

ACKNOWLEDGEMENTS

The work at IOP-CAS was supported by National Key R&D Program of China Grant (Grant No. 2018YFA0305604 & 2021YFA1401902), National Natural Science Foundation of China (NSFC) (No. 11874403), Key Research Program of Frontier Sciences, CAS, (Grant No. ZDBS-LY-SLH0010), and Beijing Natural Science Foundation (Grant No. JQ21002). The work at UBC was supported by Natural Sciences and Engineering Research Council (NSERC) of Canada and Canada Foundation for Innovation (CFI).

AUTHOR CONTRIBUTIONS

Z.G.C. and K.Z. conceived and designed the experiments, Y.Z., H.S., H.W., Y.F., and B.A.D. fabricated and measured the devices. E.G., Q.C., K.Z., and Z.G.C. analyzed and explained the data. Z.G.C. wrote the paper with comments from all other authors. Y.Z. and H.S. contributed equally to this work.

COMPETING INTERESTS

The authors declare no competing interests.

ADDITIONAL INFORMATION

Supplementary information The online version contains supplementary material available at https://doi.org/10.1038/s41535-022-00536-5.

Correspondence and requests for materials should be addressed to Ke Zou or Zhi Gang Cheng.

Reprints and permission information is available at http://www.nature.com/reprints

Publisher's note Springer Nature remains neutral with regard to jurisdictional claims in published maps and institutional affiliations.